

1
2
3
4 1 A numerical structural analysis of ducted, high-solidity,
5 2 fibre-composite tidal turbine rotor configurations in real flow
6
7 3 conditions
8
9

10 4 Mitchell G. Borg^a, Qing Xiao^{a,*}, Steven Allsop^b, Atilla Incecik^a, Christophe Peyrard^c

11
12 5 ^a*Department of Naval Architecture, Ocean, and Marine Engineering*
13 6 *University of Strathclyde*
14 7 *Glasgow, Scotland, United Kingdom*

15 8 ^b*Industrial Doctoral Centre for Offshore Renewable Energy (IDCORE)*
16 9 *University of Edinburgh*
17 10 *Edinburgh, Scotland, United Kingdom*

18 11 ^c*Electricité de France Research and Development*
19 12 *EDF R&D*
20 13 *Chatou, Ile-de-France, France*
21
22
23
24

25
26 14 **Abstract**

27 15 Establishing a design and material evaluation of unique tidal turbine rotors in true hydro-
28 16 dynamic conditions by means of a numerical structural analysis has presented inadequacies
29 17 in implementing spatial and temporal loading along the blade surfaces. This study puts
30 18 forward a structural performance investigation of true-scale, ducted, high-solidity, fibre-
31 19 composite tidal turbine rotor configurations in aligned and yawed flows by utilising out-
32 20 puts from blade-resolved, unsteady computational fluid dynamic models as boundary con-
33 21 dition loads within a finite-element numerical model. In implementation of the partitioned-
34 22 approach fluid-structure interaction procedure, three distinct internal blade designs were
35 23 analysed.

36 24 *Investigating criteria related to structural deformation and induced strains, a hydro-
37 25 static analysis is put forward in representation of the rotor at the installation depth. A
38 26 hydrodynamic analysis within aligned and yawed flow conditions is additionally undertaken.*
39 27 The resultant axial deflections for the proposed designs describe a maximum deflection-to-
40 28 bladespan ratio of 0.04, inducing a maximum strain of 0.9%. A fatigue response analysis
41 29 is undertaken to acknowledge the blade material properties required to prevent temporal
42 30 failure.

43 31 *Keywords:* structural analysis, fluid-structure interaction, high-solidity, open-centre, tidal
44 32 turbine, ducted turbine, fibre-composite

51
52
53
54
55 *Corresponding author

56 *Email addresses:* mitchell.borg@strath.ac.uk (Mitchell G. Borg), qing.xiao@strath.ac.uk (Qing
57 Xiao)

1. Introduction

Efforts to improve upon the efficacy of energy-generating turbines have been in constant development following system implementation in the global market. At the forefront of the pertinent research is the effort of increasing mass-flow through the rotor, along with the constraint and alignment of the wake flow to facilitate further turbine installations [1]. From the research attained, bi-directional ducts have been installed around a turbine rotor to enhance performance due to the acceleration of axial flow velocity through the duct throat as a result of the induced Venturi effect and pressure discrepancy between the inlet and outlet [2, 3, 4].

Attributable to the potential augmentation in power extraction as a result of the increase of mass-flow, several commercial endeavours had attempted to adopt ducted turbine technology to achieve economic prospects. Amongst the ventures, DCNS/OpenHydro Ltd. had designed an open-centre ducted design approach [5, 6]. In open-water trials, a 2 MW turbine was successfully installed in the Bay of Fundy, Canada, portrayed in Figure 1, together with a pair of 500 kW rated capacity turbines, as a demonstration array in Paimpol-Bréhat, Northern France, in collaboration with EDF France.

Albeit the enhancement in generated power, the structural response of a rotor within a bi-directional duct as a result of the flow acceleration under variant free-stream conditions, however, is largely uncertain. Few research ventures have investigated the induced rotor mechanics in relation to the developed fluid dynamics, moreover upon the implementation of a duct feature in a turbine system, within aligned or misaligned flow [7, 8, 9, 10]. The analyses had put forward coupling approaches by extracting point-force loads or pressure distributions from empirical models, blade-element momentum theory (BEMT), or two-dimensional steady-state computational fluid dynamics as loading conditions within a structural model. Albeit applicable, the approaches do not account for time-dependent variations of induced static pressure and wall shear-stress due to distinct, three-dimensional, transient fluid dynamic phenomena, such as flow separation and turbulence effects. The implementation of a duct feature further magnifies the deficiencies as a result of the rotor being succumb to ‘highly-loaded conditions’, requiring validated three-dimensional high-fidelity fluid dynamic analyses in establishing the true load distribution.

In recognition of the loading variation upon power-generating operation, this study strived to overcome the related limitations by implementing a one-way computational fluid dynamic (CFD) and finite-element analysis (FEA) coupling with blade-explicit actuality to establish a partitioned-approach fluid-structure interaction (FSI) analysis. This permitted a structural evaluation in accordance to the modelled three-dimensional flow features, together with induced turbulence effects, at the rotor. Numerical validation of the computational fluid dynamic model was attained [3] in addition to the hydrodynamic outcomes of a full-scale, ducted turbine by comparing to literature [11] and blade-element momentum theory [12]. By utilising the numerical hydrodynamic outcomes, the aim of this research was to analyse the structural performance of three distinct rotor designs for a ducted, high-solidity tidal turbine when succumb to both aligned and yawed free-stream conditions. By means of this investigation, an appropriate rotor design was acknowledged, permitting a basis onto



Figure 1: The 2 MW-rated OpenHydro ducted turbine. Adapted from [13], The Canadian Press/Andrew Vaughan, 2016.

which optimisation of the blade structure parameters may be developed.

Literature has characterised evidence of rotor loading augmentation due to a shroud installation through several decades of research by means of analytical [14], experimental [2], and numerical [3, 15, 16] analyses. Yet the conclusions have been put forward under the assumption of a rigid rotor structure. Amongst the few fluid-structure numerically-coupled ducted tidal turbine structural investigations, Nachtane et al. [7] utilised BEMT to predict the hydrodynamic performance of a bi-directional ducted tidal turbine in effort of establishing boundary conditions along the duct structure for a finite-element model. Similarly, Allsop et al. [8] implemented BEMT outputs within a structural analysis code library designed to translate individual element forces into blade stresses. This was subsequently utilised to calculate the peak stress along the blades, as well as identifying stress concentration zones, to perform survivability assessments by incorporating non-uniform inflow profiles and blade weight forces to establish the degree of cyclic stresses under distinct operating conditions for a fatigue assessment. Additionally, Luquet et al. [9] derived the pressure distribution along a ducted tidal turbine blade utilising CFD, noting that the outcome may be utilised within a finite-element analysis. Albeit providing evidence of a von Mises stress distribution along a blade, a definitive structural analysis was not put forward.

In distinction to ducted turbine analyses, a number of studies have established the fluid-structure coupling of bare turbines. The structural analyses were carried out for the purpose of material selection to distinguish between the utilisation of glass-fibre reinforced polymers (GFRPs) and carbon-fibre reinforced polymers (CFRPs) for blade spar caps and shear webs [10, 17, 18] by considering the strains induced and flapwise deflection as properties for the material selection. The hydrodynamic loads had been established by means of BEMT.

Other studies [19, 20] have considered the variation in the internal structure geometrical configuration of spar caps & shear webs by altering the number and cross-sectional profile;

1
2
3
4 100 a parametric elaboration of the results was put forward in relation to failure criteria. In
5 101 detriment of the investigation methodology, however, was the absence of high-fidelity, tran-
6 102 sient loading conditions together with the implementation of a shell-element representation,
7 103 rather than a solid-element representation. The stresses were hence induced solely along the
8 104 perimeter of the cross-section, rather than acknowledged within a three-dimensional system.
9 105 Fluid-structure interaction analyses have also been carried out by means of a monolithic-
10 106 approach methodology, where the fluid dynamic and structural mechanic modules utilise
11 107 subsequent results inherently in iterations [21, 22]. These investigations, however, have ei-
12 108 ther assumed the blade to be a solid structure, rather than varying designs or materials, or
13 109 a shell representation implementing glass-fibre composite material properties.

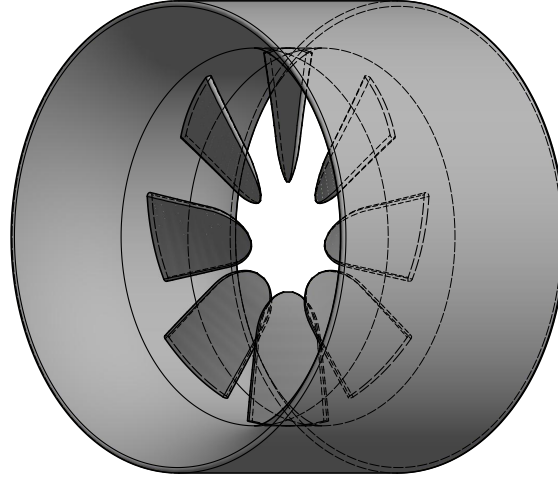
16 110 Despite the undertaken research, a finite-element analysis of a real-scale, high-solidity
17 111 rotor succumb to a variant distribution of static pressure and wall shear-stress along its
18 112 surface due to the conditional parameters of an external fluid domain, at a free-stream
19 113 vector both aligned and misaligned to the rotor axis, shall induce high degrees of numerical
20 114 complexities. This investigation evaluates the structural response of three distinct internal
21 115 blade designs as a result of the hydrodynamic effects of the duct upon the rotor, where the
22 116 individual blades are modelled as three-dimensional solid-element structures, rather than
23 117 shell-element or plate-element structures, hence inferring the outcomes in quasi-real-ocean
24 118 conditions. The numerical analysis elaborated in this present study is a continuation of
25 119 Borg et al. [3, 4], which has developed a real-scale CFD model to assess the hydrodynamic
26 120 performance of a high-solidity, open-centre rotor within a bi-directional duct for tidal turbine
27 121 applications.

33 122 **2. Numerical Methodology**

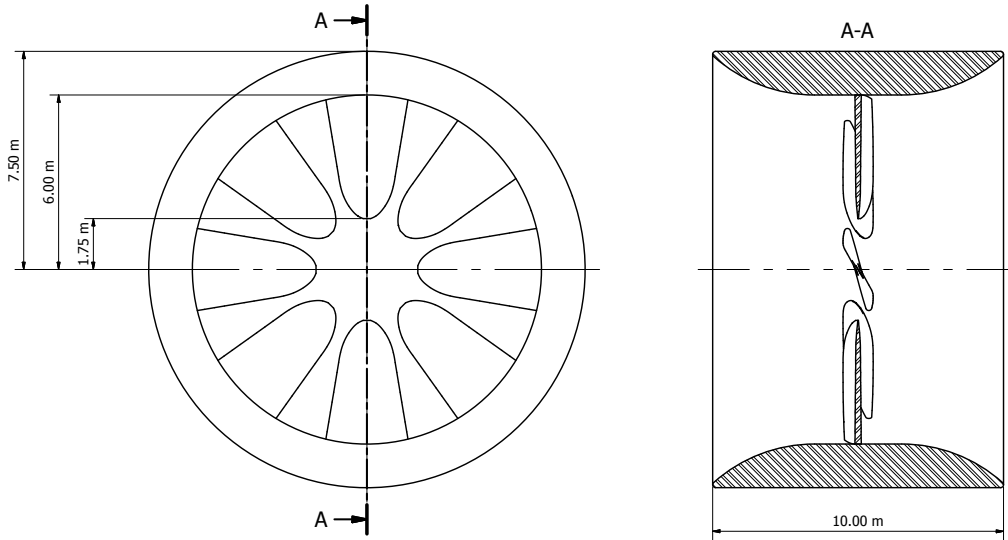
35 123 *2.1. Physical Setup*

36 124 In representation of the ducted high-solidity turbine, the dimensions described a duct
37 125 radius (R_{dct}) of 7.5 m, a rotor radius (R_{rtr}) of 6 m, a hub radius (R_{hub}) of 1.75 m, and a duct
38 126 length (L_{dct}) of 10 m, as illustrated in Figure 2. The hydrofoil sections comprising the rotor
39 127 blades consisted of a flat-plate design with rounded edges. The external hydrofoil geometry
40 128 was quasi-identical to Allsop et al. [16], yet slightly adapted to attain a more homogeneous
41 129 blade surface. The geometry was provided by EDF R&D to replicate the outcomes of a
42 130 turbine similar to the design of the OpenHydro PS2 device.

43 131 In view of the round-edged, flat-plate blade profile constituting the ducted rotor to
44 132 acquire bi-directional turbine properties, an investigation into the most appropriate internal
45 133 blade-structure design was instated. Due to the substantial chord-to-thickness aspect ratio,
46 134 unique structural configurations may be required when compared to conventional slender
47 135 blade designs. For this reason, in an effort to acquire an efficacious internal blade design in
48 136 terms of specific mass, material cost, and structural response of the rotor blades, three design
49 137 variations were investigated in replication of turbine blade designs elaborated in Ref. [23]:
50 138 (a) a solid blade consisting of a single material throughout its volume, (b) a cored blade
51 139 consisting of a thick shell with a foam core, and (c) a reinforced blade consisting of a thick
52 140 shell with webbing reinforcements in a void core, oriented perpendicular to the blade chord



(a) Rendered three-dimensional CAD representation



(b) First-angle sectioned projection

Figure 2: Geometrical model of the ducted tidal turbine

141 along the entire blade length, which has been water-flooded upon installation, as illustrated
 142 in Figure 3. The implemented shell and reinforcement thicknesses of the two latter blade
 143 designs were instituted to be one-fourth of the blade profile thickness down the entire blade
 144 as a proximate median value from rotor composite cross-section evaluations by Grogan et
 145 al. [17]. In addition, the distance between each shear web reinforcement (d_{rein}) was acquired
 146 by means of:

$$d_{rein} = \frac{c_{rtr} - 2t_{rtr}}{3} \quad (1)$$

147 where c_{rtr} is the cross-section chord length and t_{rtr} is the cross-section thickness.

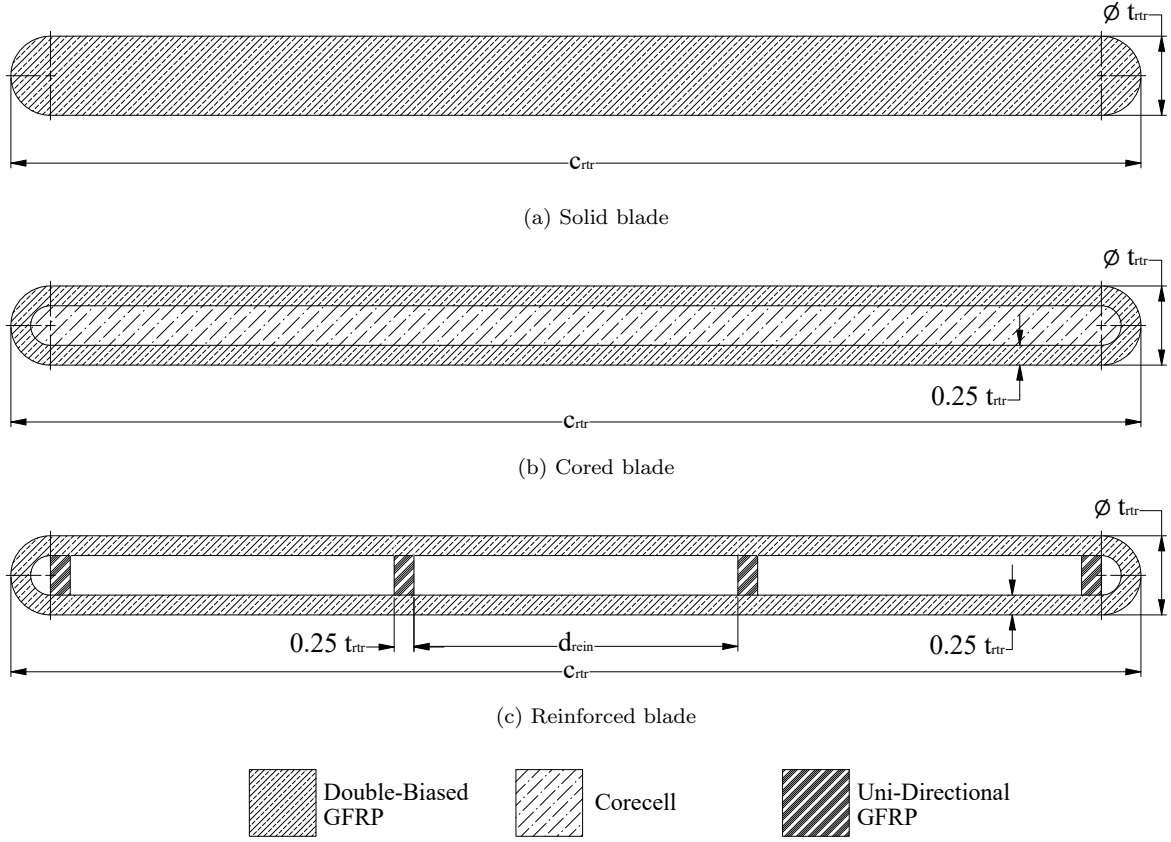


Figure 3: Cross-sectional representations of the high-solidity rotor blade designs considered for the structural analyses

Table 1: High-solidity blade material properties [17]

Material	E_1 (GPa)	E_2 (GPa)	G_{12} (GPa)	ν_{12}	Density ($\text{kg}\cdot\text{m}^{-3}$)	Design
DB GFRP	22.0	22.0	2.7	0.30	1850	a, b, c
Corecell	0.044	0.044	0.020	0.30	65	b
UD GFRP	38.8	10.0	2.7	0.28	1950	c

The materials considered for the structural analysis comprised of composite materials that are commonly utilised in the tidal turbine industry [17]: (i) double-biased (DB) orthotropic glass-fibre reinforced polymers (GFRP), employed for the solid blade design and the shell segments of the cored & reinforced blade designs; (ii) uni-directional (UD) anisotropic glass-fibre reinforced polymers, employed for the shear web reinforcement segments of the reinforced blade design; and (iii) corecell structural foam for the core segment of the cored blade design. The properties of the listed materials are presented in Table 1.

A select range of hydrodynamic conditions was considered for the analysis. Within

1
2
3
4 156 aligned flow conditions, low, mean, and extreme currents were considered at 1 m.s^{-1} , 4
5 157 m.s^{-1} , and 7 m.s^{-1} , respectively. In addition, a bearing range of 0° , 15° , 23.2° , 30° , solely
6 158 at 4 m.s^{-1} , was considered within yawed flow conditions. Both analyses were conducted at
7 159 low, nominal, and high rotational velocities (TSR 1.00, 1.75, and 2.50). The simulations
8 160 implemented an inlet turbulence intensity of 3% and an inlet turbulent length scale of 1
9 161 m. At these conditions, the rotor designs were assessed on distinct criteria: (i) geometric
10 162 characterisation, (ii) structural deflection, (iii) fracture response, (iv) capital cost, and (v)
11 163 fatigue response to establish a definitive blade design selection for efficacious implementation
12 164 within tidal turbine operation.

15 165 *2.2. Numerical Setup*

16 166 Having established a validated computational fluid dynamic model for the hydrodynamic
17 167 analysis of a ducted, high-solidity tidal turbine [3], the structural response of the rotor
18 168 blades by means of a finite-element analysis was considered. A partitioned-approach fluid-
19 169 structure interaction (FSI) model was therefore set up, where the hydrodynamic solver
20 170 was coupled with the structural solver by extracting the outcomes attained from the prior
21 171 model and implemented as loading boundary conditions within the latter. In consideration
22 172 of this technique, each of the rotor blades, disassociated from the duct, was individually
23 173 modelled within the finite-element solver utilising the ducted turbine blade geometrical
24 174 profiles employed within the fluid dynamic solver.

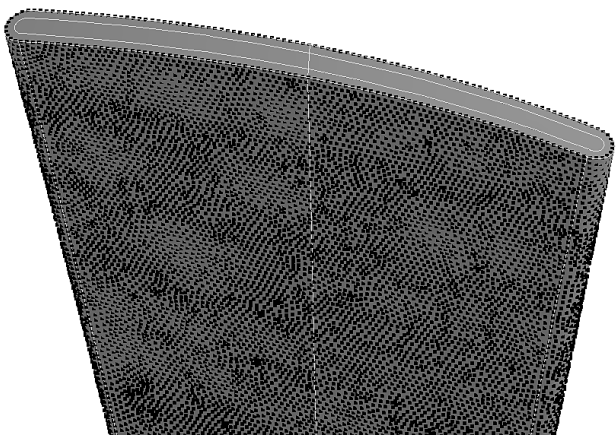
25 175 A one-way FSI analysis was favoured due to three factors: (i) the internal blade structure
26 176 was required to be altered, hence varying the response properties of the structure; (ii) the
27 177 non-slender physicality of the high-solidity blades may exhibit high structural stiffness; and
28 178 (iii) as the extremities of the blades are fixed at the duct, where the highest dynamics
29 179 are induced, the structural response may not be significant. Due to the incorporation of
30 180 a one-way approach, the loading data was therefore identical for each blade design upon
31 181 implementation.

32 182 *2.2.1. Partitioned-Approach Fluid-Structure Framework*

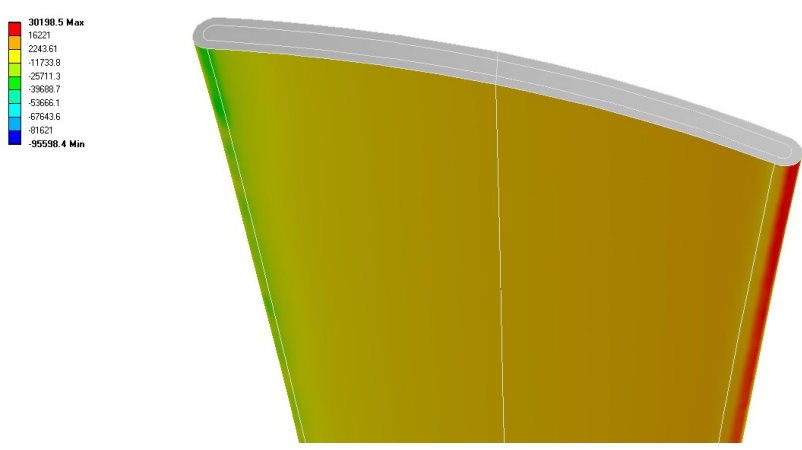
33 183 In an effort to constitute the one-way fluid-structure interaction framework, the boundary
34 184 conditions inducing a loading distribution along the blade surfaces were instated from the
35 185 distributions of static pressure and wall shear-stress attained within, and imported directly
36 186 from, the hydrodynamic model at distinct temporal points along the turbine rotation. The
37 187 hydrodynamic model described a three-dimensional, real-scale, unsteady CFD model that
38 188 coupled the seven-equation Reynolds-Stress ‘Stress-Omega’ Model (τ - ω) turbulence model
39 189 to close the Navier-Stokes equation and analyse the anisotropic flow domain [24]. The
40 190 structural model described a three-dimensional solid quasi-static linear model. Each of the
41 191 eight blades was therefore modelled independent from the entire system, upon which unique
42 192 loading conditions were imposed. The setup hence permitted an autonomous blade-resolved
43 193 fluid-structure interaction analysis of the blade designs, unique for the tidal turbine, within
44 194 a range of environmental conditions.

45 195 The partitioned coupling from the hydrodynamic solver to the structural solver consisted
46 196 of exporting data points detailing the Cartesian location and value of the parameters spec-

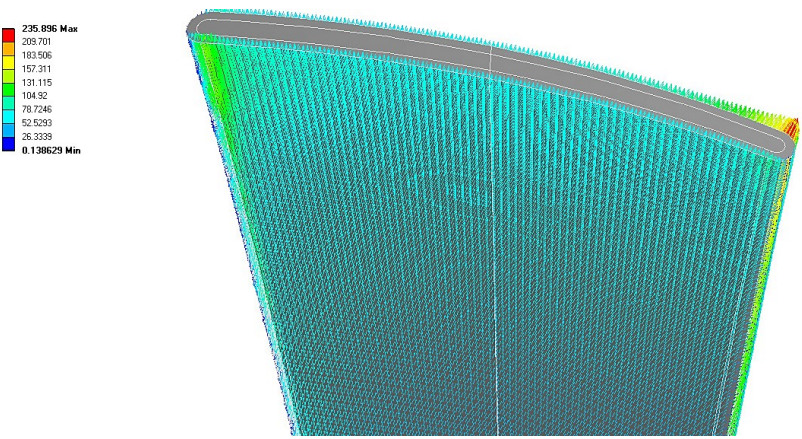
1
2
3
4
5
6
7
8
9
10
11
12
13
14
15
16
17
18
19
20
21
22
23
24
25
26
27
28
29
30
31
32
33
34
35
36
37
38
39
40
41
42
43
44
45
46
47
48
49
50
51
52
53
54
55
56
57
58
59
60
61
62
63
64
65



(a) Distribution of input source points along the blade surface



(b) Static pressure input boundary condition ($U_\infty = 7 \text{ m.s}^{-1}$; $TSR = 1.75$; $\phi = 0^\circ$)



(c) Wall shear-stress input boundary condition ($U_\infty = 7 \text{ m.s}^{-1}$; $TSR = 1.75$; $\phi = 0^\circ$)

Figure 4: Illustration of the partitioned-approach fluid-structure interaction technique implementation by importing parameter distributions along the blade surface from the hydrodynamic CFD model

1
2
3
4 197 ified. As the total force induced by a fluid flow is the summation of static pressure and
5 198 wall shear stress upon a surface, the two parameters were extracted from the CFD solver.
6 199 Within the finite-element model, static pressure was imposed as a magnitude, whereas wall
7 200 shear-stress was imposed as a Cartesian vector (x-,y-, and z-wall shear). On average, 55,000
8 201 data points per time-step were transferred; the implementation is illustrated in Figure 4.
9 202 The parametric distribution at the rotor surface was imported **at every azimuth angle (ϕ)**
10 203 **of 45° along the rotation** for three periods to attain a representation of the dynamic load
11 204 induced upon operation.

12
13
14 205 In addition to the hydrodynamic parameters, hydrostatic pressure was introduced within
15 206 the solution by modelling the rotor axis to be situated 20 m below sea-level due to the ducted
16 207 tidal turbine design conditions of being installed at 35 m depth [25]. Furthermore, fixed
17 208 boundary conditions were allocated to the root surface of the blade, together with Coriolis
18 209 effect considered at constant rotational velocity, to acquire representative environmental
19 210 conditions of the ducted, high-solidity tidal turbine in operation.

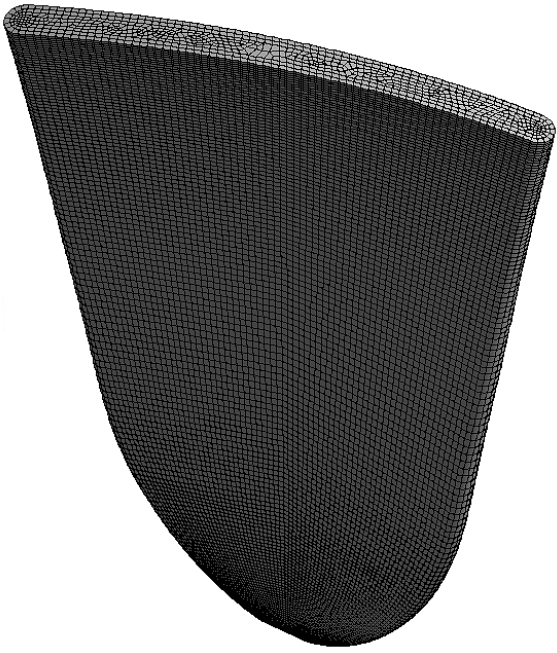
21 22 211 *2.2.2. Finite-Element Mesh*

23 212 Designed to explicitly incorporate all eight distinct rotor blades for the three blade de-
24 213 signs, the physical models were imprinted with a hybrid hexahedral-tetrahedral mesh for
25 214 the solid and cored blade design, and a hexahedral mesh for the reinforced blade design,
26 215 illustrated in Figure 5. Both physical models consisted of solid quadratic elements. The
27 216 implementation of solid elements was preferred to shell elements in representing the outer-
28 217 shell segment of the blade as shell elements put forward the assumption that the structural
29 218 outcomes are consistent throughout the structure thickness. This was deemed to be unten-
30 219 able for the full-scale high-solidity rotor due to the complex geometrical layout of the blade,
31 220 together with the variable parametric distribution upon its surface.

32
33 221 In addition to a solid-element format, quadratic elements were utilised to introduce mid-
34 222 nodes within each cell. The implementation was advantageous in discretising the thickness
35 223 of the outer-shell & reinforcement structures to increase the accuracy of the simulation.
36 224 Furthermore, a two-cell-thick layout was imposed along the thickness of the shell & rein-
37 225 forcement sections, as illustrated in Figure 5b, to attain a quadratic relationship between
38 226 the structural outcomes and the thickness of the blade feature; hexahedral volumetric cells
39 227 were imposed along all exposed surfaces for all blade designs.

40 228 In creating the mesh, the solid and cored blades were instated as whole components for
41 229 the mesh to be imposed along; the same mesh was utilised, yet differing material properties
42 230 were allocated for the two cases. The reinforced blade, however, was more complex to set up.
43 231 To permit an equivalent distribution of hexahedral cells, the structure was discretised into
44 232 blade sections. Yet, due to the discretisation, the three-dimensional non-uniform rational
45 233 basis spline (NURBS) sectioned structure was too complex to tessellate in a consistent
46 234 manner. In consequence, the sections were meshed separately, and numerically linked by
47 235 means of a face-to-face bonded contact merge when simulating. Overall, the eight rotor
48 236 blades were meshed, where the solid/cored rotor mesh was comprised of a total of 635,672
49 237 elements and 2,680,248 nodes, whereas the reinforced rotor comprised of 571,392 elements
50 238 and 3,362,160 nodes. A mesh independence procedure, described in Table 2, was carried out

1
2
3
4
5
6
7
8
9
10
11
12
13
14
15
16
17
18
19
20
21
22
23
24
25
26
27
28
29
30
31
32
33
34
35
36
37
38
39
40
41
42
43
44
45
46
47
48
49
50
51
52
53
54
55
56
57
58
59
60
61
62
63
64
65



(a) Geometric tessellation of the solid & cored blade profiles



(b) Geometric tessellation of the reinforced blade profile

Figure 5: Illustration of the blade meshes

on the duct domain by considering the parameter with the highest degree of dynamics. Mesh independent parameters were established utilising ITTC recommended meshing procedures

and guidelines [26]:

$$\varepsilon_n = S_n - S_{n-1} \quad (2)$$

$$\Psi = \frac{\varepsilon_n}{\varepsilon_{n-1}} \quad (3)$$

where Ψ is the convergence ratio, ε is the difference between the considered variable (S) at different mesh independence study iterations, and the subscript n is the mesh independence study iteration.

Table 2: Mesh independence analysis for the solid/cored rotor blade structural design

n	Cell Number	Cell Number Ratio	S	ε	Ψ
3	635,672	1.242	0.002528	-0.000030	0.2451
2	511,834	1.340	0.002498	-0.000122	
1	382,167		0.002376		

The finite-element computations were performed using the ARCHIE-WeSt cluster facility at the University of Strathclyde by running two Intel Xeon Gold 6138 2.00 GHz computational nodes, with 8 cores and up to 192 GB of RAM per node per simulation. One ducted rotor structural simulation was completed within roughly 20 wall-clock hours, equivalent to 160 core-hours.

3. Numerical Model Characterisation

3.1. Physical Modelling

In consideration of the analysis of a physical turbine, notable definitions concerning the resultant performance outcomes were identified. The tip-speed ratio (TSR) was established as an equivalence between the linear blade-tip velocity and the free-stream velocity (U_∞):

$$TSR = \frac{\Omega_x R_{rtr}}{U_\infty} \quad (4)$$

where Ω_x is the system axial rotational speed and R_{rtr} is the rotor radius.

The thrust coefficient (C_T) was quantified as a function of the device thrust (T_{dvc}) and the maximum thrust potentially induced upon the device area (T_∞):

$$C_T = \frac{T_{dvc}}{T_\infty} = \frac{F_z}{\frac{1}{2}\rho A_{dvc} U_\infty^2} = \frac{F_z}{\frac{1}{2}\rho\pi R_{dvc}^2 U_\infty^2} \quad (5)$$

where ρ is the fluid density, A_{dvc} is the device area, R_{dvc} is the device radius, and F_z is the stream-wise axial force on the device.

In establishing the fatigue life of the materials constituting the blades, the strain-life method was utilised to relate the temporal structural response:

$$\frac{\Delta\varepsilon_e}{2} = \frac{\sigma'_f}{E} \cdot (2N_f)^b \quad (6)$$

where $\Delta\varepsilon_e$ is the total strain amplitude, σ'_f is the fatigue strength parameter, E is the Young's modulus, N_f is the number of cycles to failure, and b is the fatigue strength exponent.

4. Structural Performance of the Ducted, High-Solidity Tidal Turbine Rotor

4.1. Geometric Characterisation

Primarily acknowledging the variations in geometric characteristics between the blade designs, three properties were investigated: the moment of inertia, specific mass, and specific gravity of the high-solidity rotors.

As specified in Table 3, the solid blade design attained the highest parametric values. This design required the highest degree of torque to induce a unit rotational acceleration. In contrast, the cored blade design attained the lowest parametric values as half of the dense GFRP volume was substituted for the Corecell material. The reinforced design, consisting of two GFRP materials for the shell and webs, whilst flooded with water, presented intermediate values between the two prior designs.

4.2. Hydrostatic Analysis

Hydrostatic pressure was implemented along the surfaces of the blades in simulation of the subsea depth. The suitability of the structures was therefore acknowledged throughout non-operational procedures, such as installation and maintenance processes.

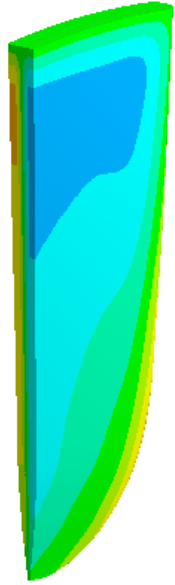
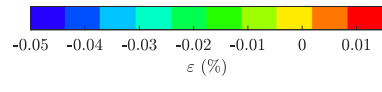
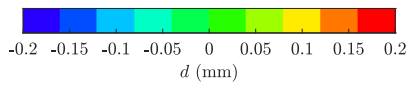
By means of the analysis, the solid and reinforced blade designs sustained their structural integrity as no structural deviation was induced. The cored blade, however, was succumb to minute yielding, due to the malleable foam-core, which induced a region of low strain at the root, as illustrated in Figure 6.

4.3. Hydrodynamic Performance Analysis

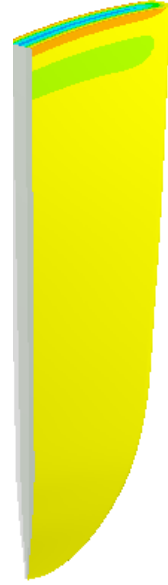
The hydrodynamic thrust induced upon the ducted turbine rotor during operation within aligned and yawed flow conditions was analysed, as illustrated in Figure 7a and Figure 7b, respectively. Within aligned flow conditions, a high thrust coefficient was attained at low TSR, with a mean value of 0.76, which decreased to a mean of 0.52 at high TSR in a linear variation. The outputs at yawed flow conditions acted similarly, yet portrayed a deviation dependent on the angular bearing of the free-stream. The highest thrust was attained at a flow-bearing of 23.2° . Further descriptions are elaborated in Ref. [3].

Table 3: Geometric properties of the high-solidity tidal turbine rotor designs

Blade Property	Solid Design	Cored Design	Reinforced Design
Moment of Inertia ($\text{kg}\cdot\text{m}^2$)	4.587×10^5	2.422×10^5	3.640×10^5
Specific Mass ($\text{kg}\cdot\text{m}^{-3}$)	1850	982	1472
Specific Gravity	1.853	0.984	1.475

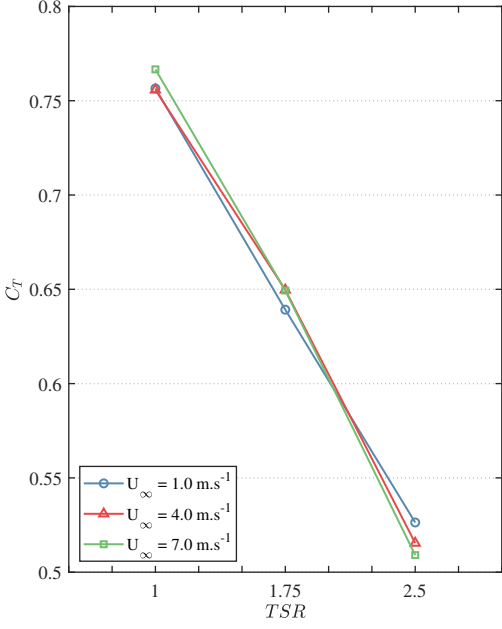


(a) Axial deflection

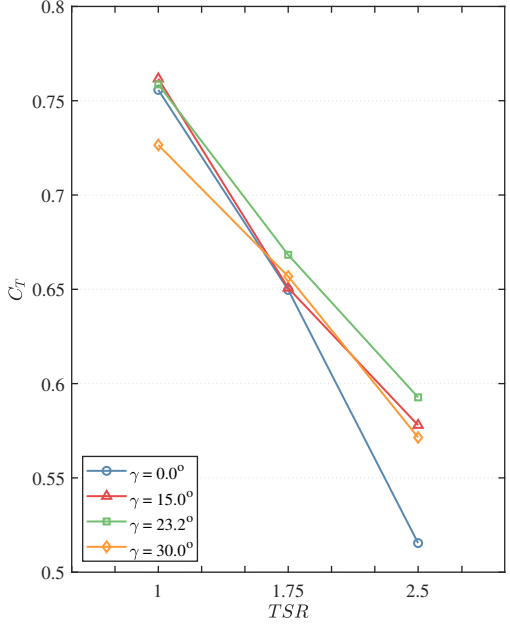


(b) Radial strain distribution

Figure 6: Structural response cross-section of the cored blade design under hydrostatic load



(a) Aligned Flow Conditions



(b) Yawed Flow Conditions

Figure 7: Mean hydrodynamic thrust coefficient upon the turbine rotor at aligned and yawed flow conditions

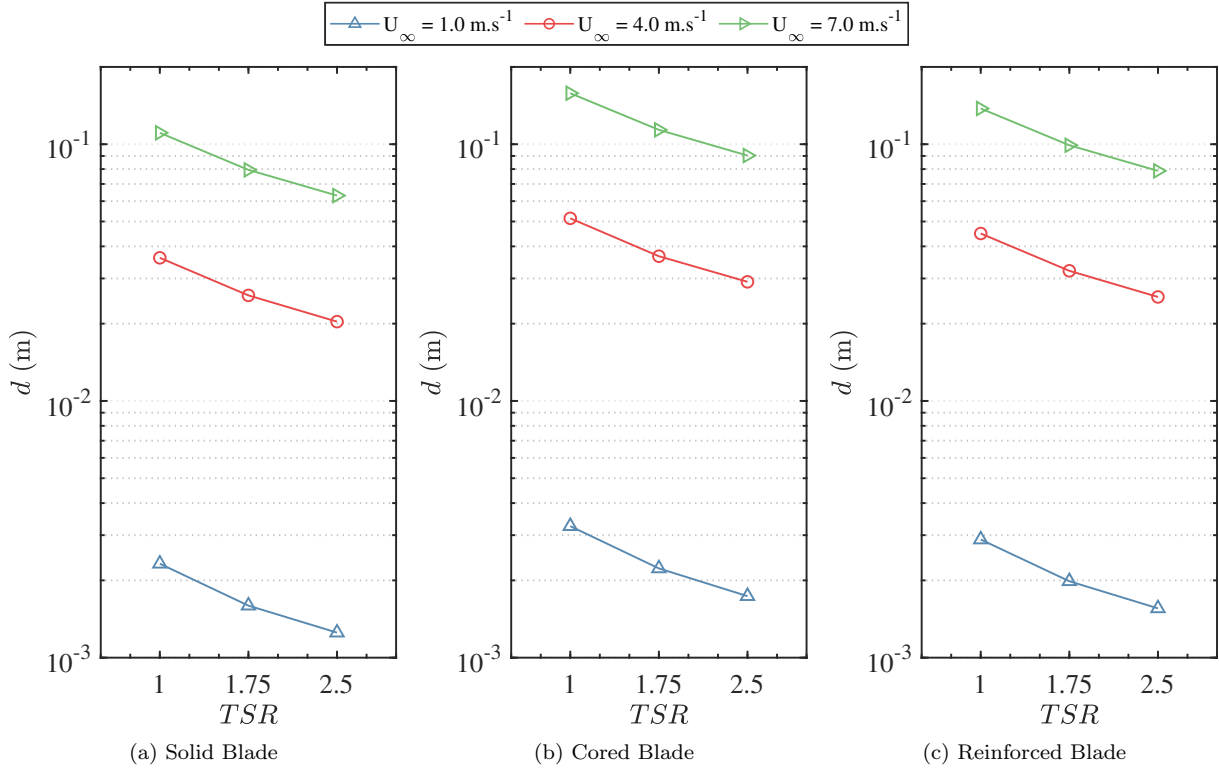


Figure 8: Mean axial deflection of the distinct blade designs within aligned flow conditions

4.4. Hydrodynamic Fracture Analysis

4.4.1. Blade Deflection

4.4.1.1 Axial Deflection

Primarily, the blade deflection acting parallel to the rotor axis was analysed in relation to the free-stream magnitude and turbine rotational velocity for all three blade designs. Illustrated in Figure 8, the solid blade attained the lowest mean deflection, whereas the cored blade acquired the highest, albeit minutely, due to the implementation of the foam core, which constituted 50% of the blade volume, diminishing the global Young's modulus. The reinforced blade attained an intermediate mean deflection.

The axial deflection was relatively minute for all three designs, with a maximum deflection equivalent to approximately 4% of the blade length. The deflections were minute as the blade was constrained at the tip, where higher dynamics were induced, rather than at the hub. At yawed flow conditions, the deflections of the blade were more substantial at higher TSRs, as illustrated in Figure 9, analogous to the variation in thrust.

The behaviour of the deflection along the blade surface was investigated. As illustrated in Figure 10, the maximum value was attained at the trailing edge in the vicinity of the blade hub. The point of highest deflection was present at this location as a result of the relatively high blade pitch, inducing simultaneous bending and torsion upon the structure.

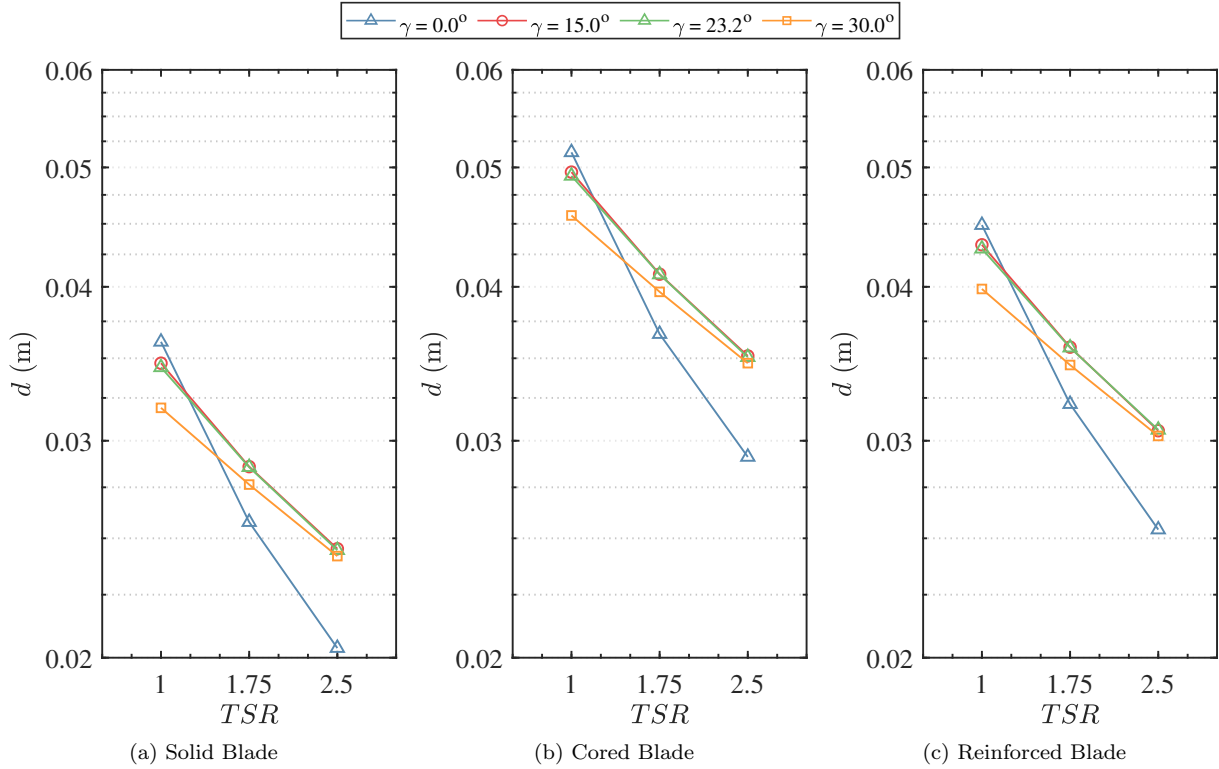


Figure 9: Mean axial deflection of the distinct blade designs within yawed flow conditions

4.4.1.2 Global Deflection

To acknowledge the proportion of axial deflection upon the full physical response, the three-dimensional global deflection of the blades was acquired, illustrated in Figure 11. On average, for both aligned and yawed flow conditions, the axial deflection was found to be approximately 94% of the total deflection, hence acknowledging the majority of the dynamics induced to be acting within the axial direction of the rotor.

4.4.2. Normal Elastic Strain

4.4.2.1 Radial Strain

Establishing the strain acting along the length of the blades, the lowest values of radial strain were attained by the solid blade design, as illustrated in Figure 12. The highest values were displayed by the cored blade due to the comparably lesser rigidity, with an intermediate value by the reinforced blade. The maximum radial strain along the blade diminished with rotational velocity, yet increased in relation to the free-stream velocity, analogous to the thrust variation induced upon the blade. The cored design response at low free-stream conditions was acknowledged to be distinct from the supplementary two blade designs due to the strain induced by the hydrostatic pressure. In addition, the maximum strain response induced at yawed flow conditions occurred at flow bearings of 15° and 23.2° for all blade designs, as depicted in Figure 13.

The highest tensile value transpired upon the cored blade at low rotational velocity in

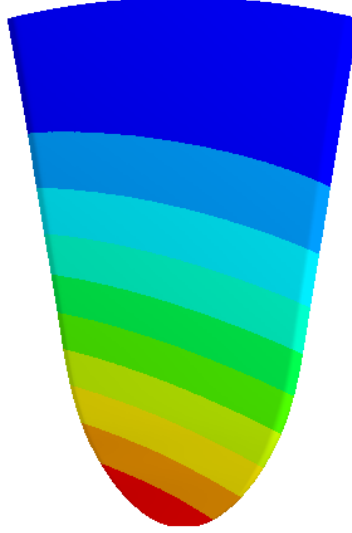
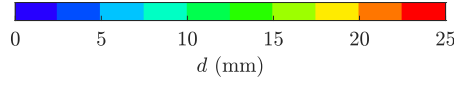


Figure 10: Illustration of the axial deflection distribution along the solid blade design ($U_\infty = 4 \text{ m.s}^{-1}$; $TSR = 1.75$; $\phi = 0^\circ$)

extreme free-stream conditions. The magnitude was 22.1% of the DB GFRP yield strength, hence not exceeding its ultimate strain-to-failure value. To ascertain its structural integrity, an engineering safety factor of 2 was implemented, increasing the normal strain to 44.2% of the permissible strain. Operation at the specified conditions was therefore inconsequential to the structural integrity of the rotor, and within the limits of reliable operation.

Furthermore, in recognising the radial strain distribution along the surfaces of the three blade designs, illustrative representations of the structures were established, as depicted in Figure 14. By means of the analysis, two strain concentrations, in tension and compression, were acknowledged towards the leading edge, at the root, of the high-solidity blade for all three structural designs in both aligned and yawed flows. The concentration was brought about due to the simultaneous bending and torsion instigated by the fluid-structure interaction upon the wide blade. Consequent to the presence of strain localisation, should a structural defect transpire, crack propagation may induce the structural failure of the high-solidity blade.

In addition, the illustrated surface strain distribution of the three blades were distinct in relation to the internal design. The solid blade attained a comparatively large concentration zone, which dissipated gradually along the structure. The cored blade sustained a higher degree of strain concentration along the root of the rotor. The reinforced blade permitted global strain reduction, yet induced local strain increases at the locations of the reinforcement webs.

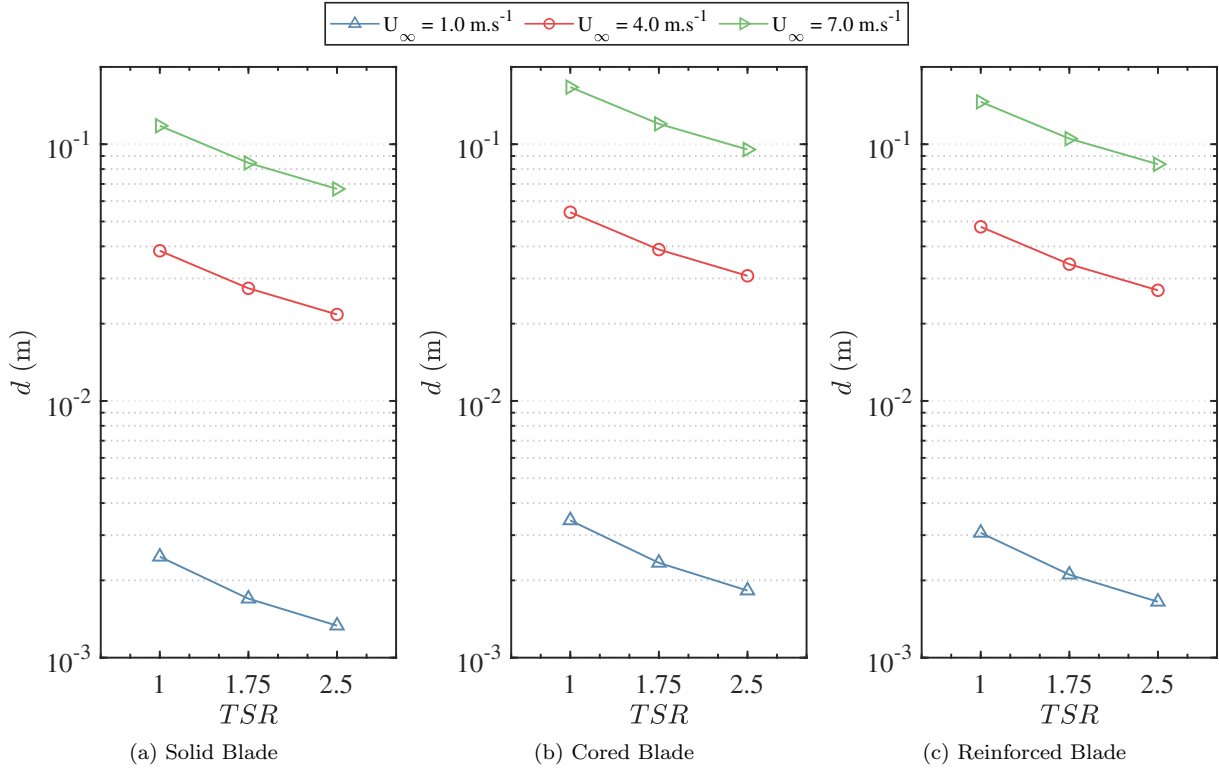


Figure 11: Mean global deflection of the distinct blade designs within aligned flow conditions

4.4.2.2 Tangential Strain & Axial Strain

Identifying strain acting along the width of the blade, illustrated in Figure 15, the values of tangential strain were found to be, on average, a magnitude of 3, for solid blades, and 15, for cored and reinforced blades, lower than the radial strains. The lowest values of tangential strain were attained by the reinforced blade design, whereas the highest values were displayed by the solid blade design. Due to the orthotropic material consistency of the blade setup, the higher rigidity permitted lessened stress dissipation in comparison to the variant designs. Similar to the variation in hydrodynamic thrust induced upon the blade, the tangential strain along the blade diminished with rotational velocity, whilst increasing with free-stream velocity.

Identifying strain acting in a direction parallel to the rotor axis, illustrated in Figure 16, the values of axial strain were found to be, on average, a magnitude of 3, for solid blades, and 13, for cored and reinforced blades, lower than the radial strain. The variations in structural outcomes displayed similarities with those of tangential strain.

4.4.3. Equivalent Elastic Strain

As the structural response of the high-solidity rotor pertained multi-directional strain states, the von Mises equivalent elastic strain was analysed. The lowest values of equivalent strain were attained by the solid blade design, whereas the highest values were displayed by the cored design due to the lesser rigidity. The reinforced design attained an intermediate

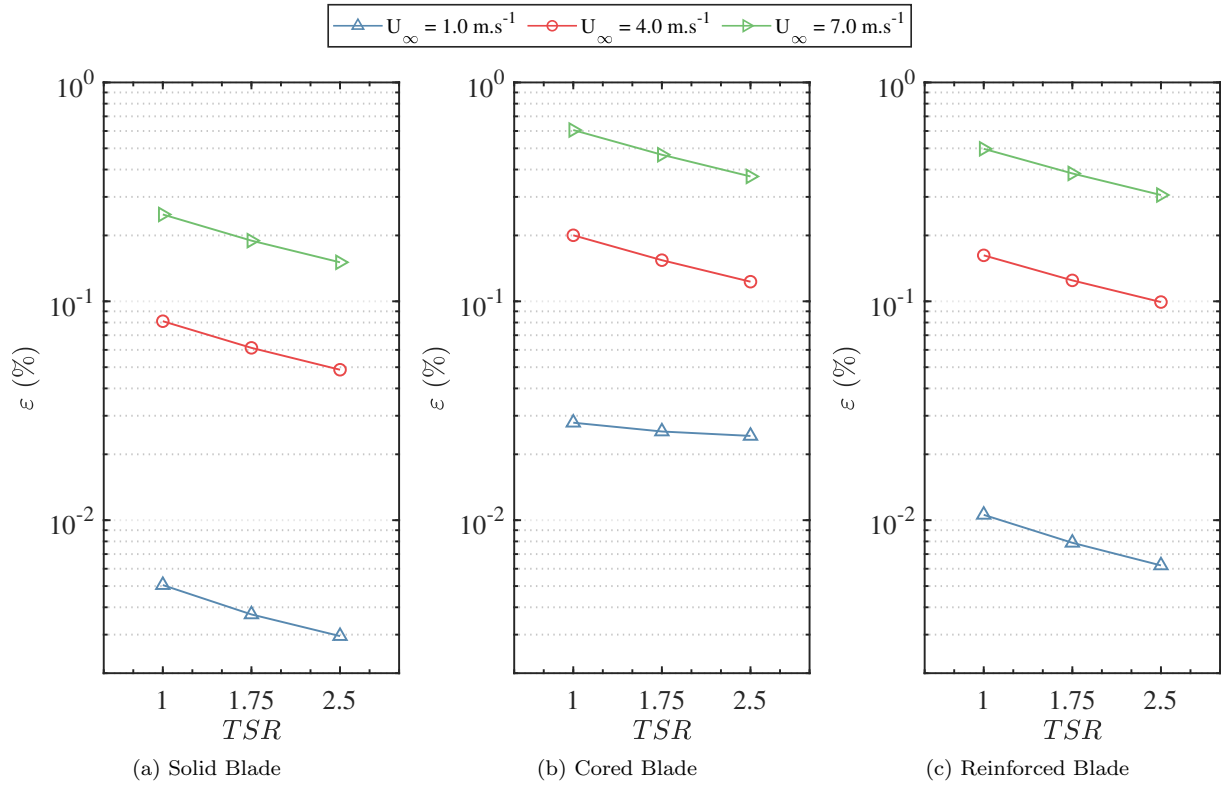


Figure 12: Mean normal radial strain of the distinct blade designs within aligned flow conditions

response, as illustrated in Figure 17. As a result of the degree of strain, the maximum tensile value increased to 67.8% of the DB GFRP yield strength.

4.4.4. Shear Elastic Strain

The ducted tidal turbine design consisted of rotor blades sharply extruding from the duct housing at the tip of the structure, where dynamics are highest. The induced shear strain was therefore investigated at the interfacing plane between the blade root and the duct.

Illustrated in Figure 18, the value of shear response was found to be equivalent in magnitude to the radial and equivalent strain, as the strain concentrations were present within the vicinity of the blade root. The shear distribution along the root plane at mean aligned velocity was investigated for the three blade designs, illustrated in Figure 19. Along the three blade profiles, four concentration zones were developed at the rounded vertices of the root plane as torsion and bending motions were induced.

4.5. Material Cost Analysis

In result of the outcomes attained via the prior investigations, the structural integrity of the three proposed internal blade designs was sustained within the analysed conditions. To establish a distinction between the designs, a material cost analysis was put forward, acknowledging the most cost-effective composition, in exclusion of manufacturing and fabrication costs.

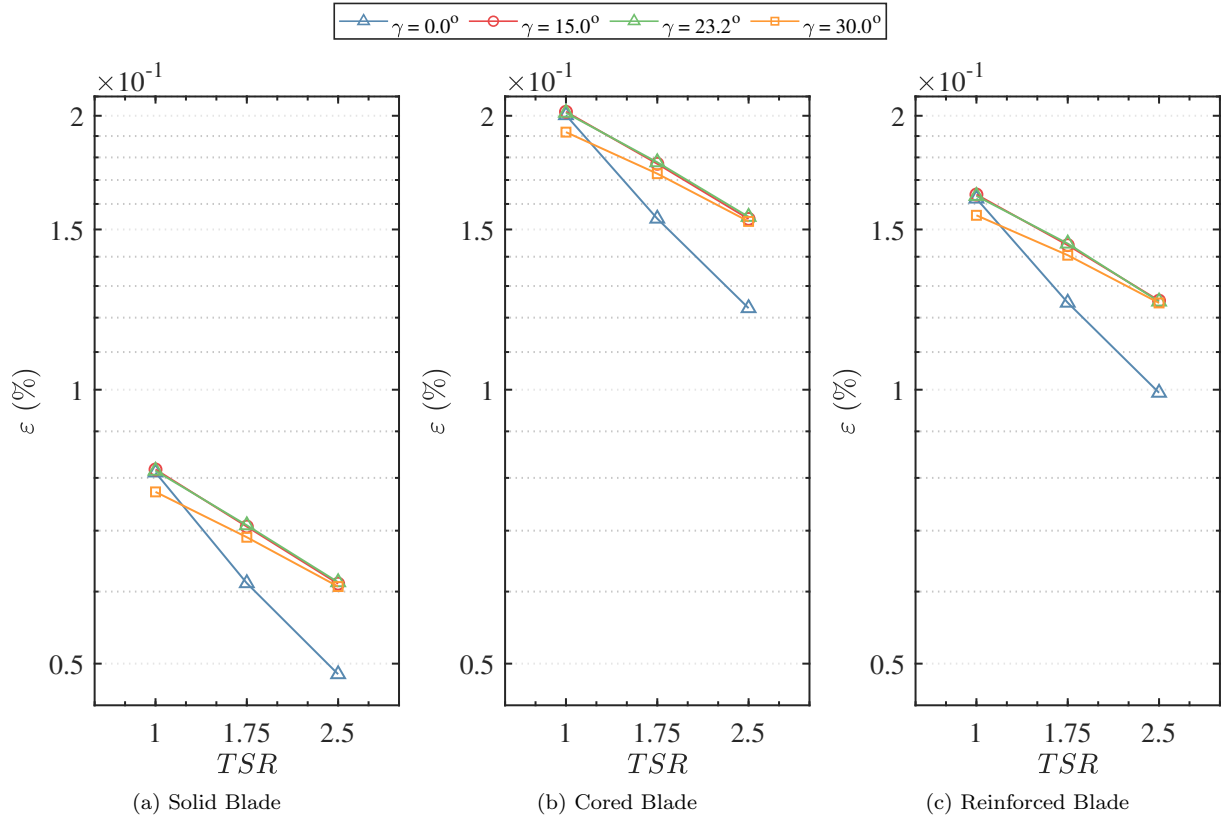
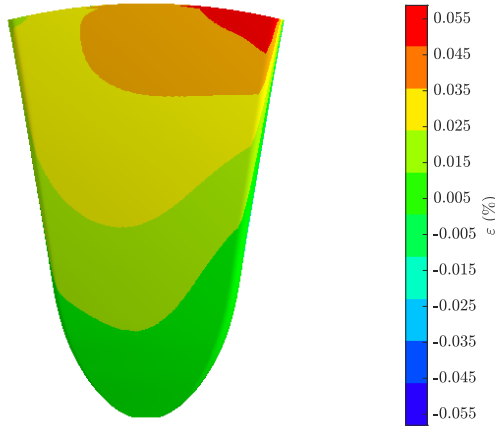


Figure 13: Mean normal radial strain of the distinct blade designs within yawed flow conditions

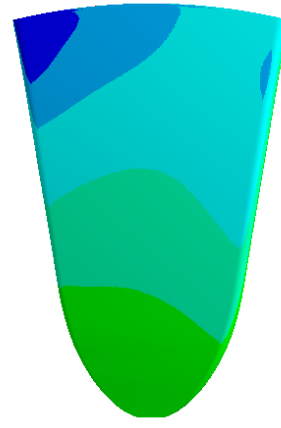
Implementing material costs for uni-directional fibre sheets, bi-directional fibre sheets, epoxy resin, and structural foam materials from prior investigations [27], whilst attaining the volume of the blade components from the established structural model, the final costing estimations of the blade materials for the full rotor was established, as depicted in Table 4. The ratio of filler-to-matrix materials within the GFRPs was acquired by relating the densities of the matrix [28] and e-glass to the global density of the fibreglass material. The most cost-effective arrangement, in terms of materials implemented, was found to be the reinforced design, being approximately 50% and 6.5% lower in capital than the solid and cored blade designs, respectively.

Table 4: Total material costs of the high-solidity tidal turbine rotor designs

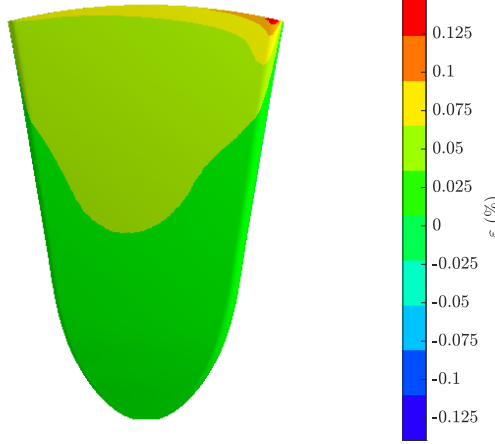
Blade Structure	Solid Design	Cored Design	Reinforced Design
Cost (\$)	596,000	321,000	300,000



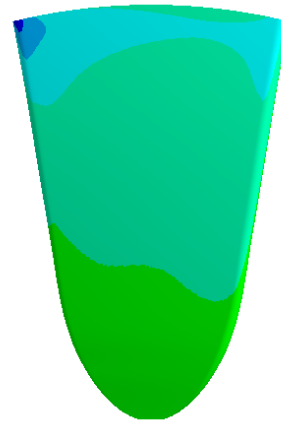
(a) Solid Blade (Pressure Side)



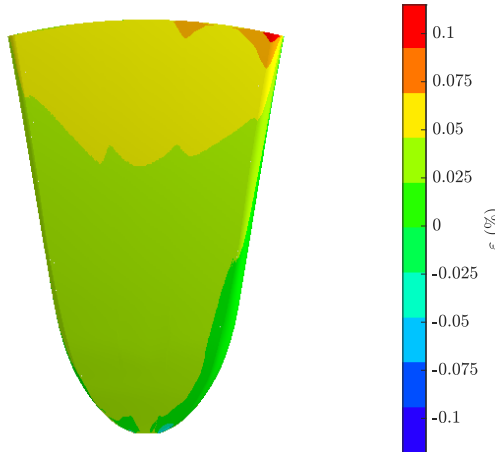
(b) Solid Blade (Suction Side)



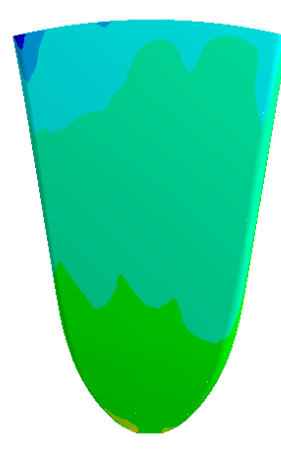
(c) Cored Blade (Pressure Side)



(d) Cored Blade (Suction Side)



(e) Reinforced Blade (Pressure Side)



(f) Reinforced Blade (Suction Side)

Figure 14: Illustrations of the normal radial strain distribution along the blade structural designs ($U_\infty = 4$ m.s⁻¹; $TSR = 1.75$; $\phi = 0^\circ$)

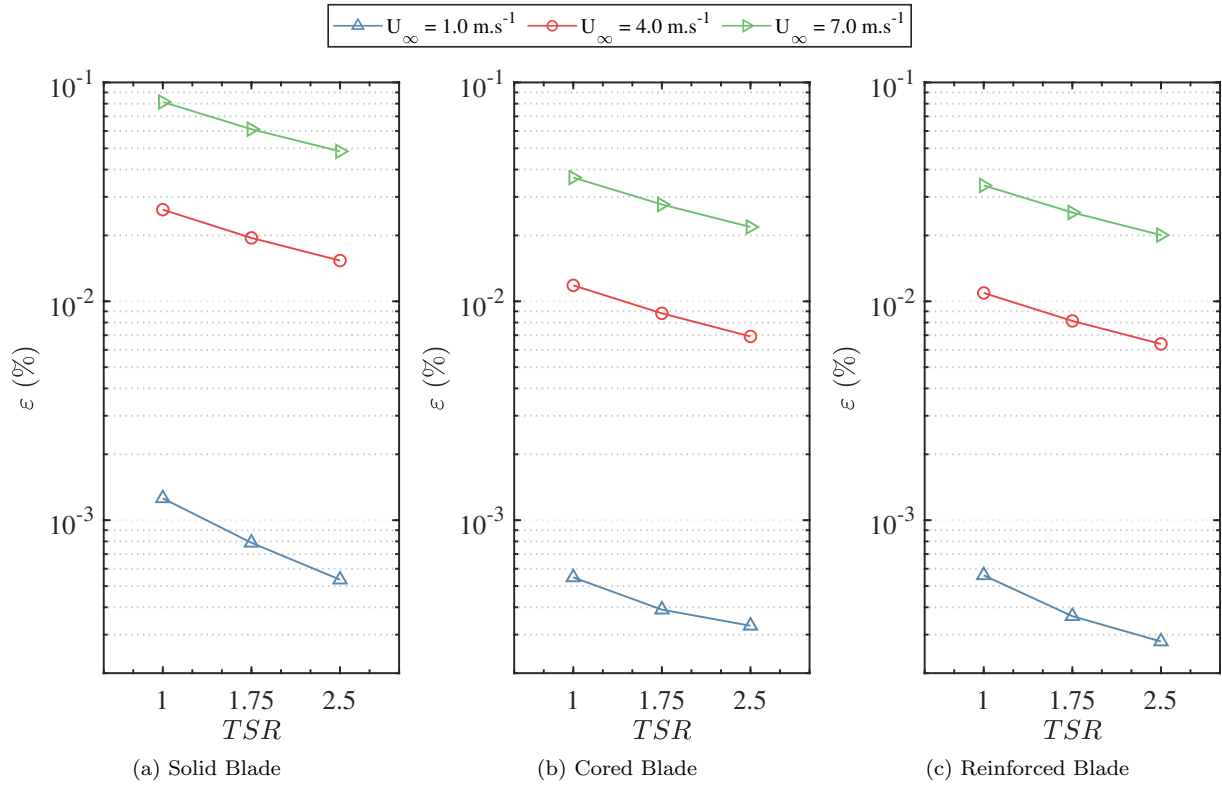


Figure 15: Mean normal tangential strain of the distinct blade designs within aligned flow conditions

4.6. Fatigue Analysis

4.6.1. Principal Elastic Strain

In establishing the characteristics that lead to temporal failure as a result of fatigue crack propagation, the maximum principal strain along the blade was investigated. Analysed at the considered azimuth positions at mean free-stream magnitude (4 m.s⁻¹) within aligned (0°) and nominal bearing (23.2°) at mid and high rotational velocities, the mean response per azimuth angle of 45° was attained. **Due to the inconsistencies in the strain response of the cored blade design at low free-stream velocity, the fatigue analysis was solely undertaken upon the solid and reinforced blade designs.** By means of the investigation, a cyclic response was acknowledged, as illustrated in Figure 20, providing evidence of the likelihood of failure by fatigue.

4.6.2. Strain-Life Analysis

As a cyclic load was induced within a rotational period of power-generating operation, an investigation into the fatigue performance of the fibre-composite rotor blade designs was carried out. Analysing the system when succumb to high-cycle fatigue, the strain-life ($\epsilon_e - N_f$) methodology was implemented to establish the temporal response of the ducted turbine rotor within a 10- to 25-year design-life.

The strain-life approximation however requires specifications related to the failure prop-

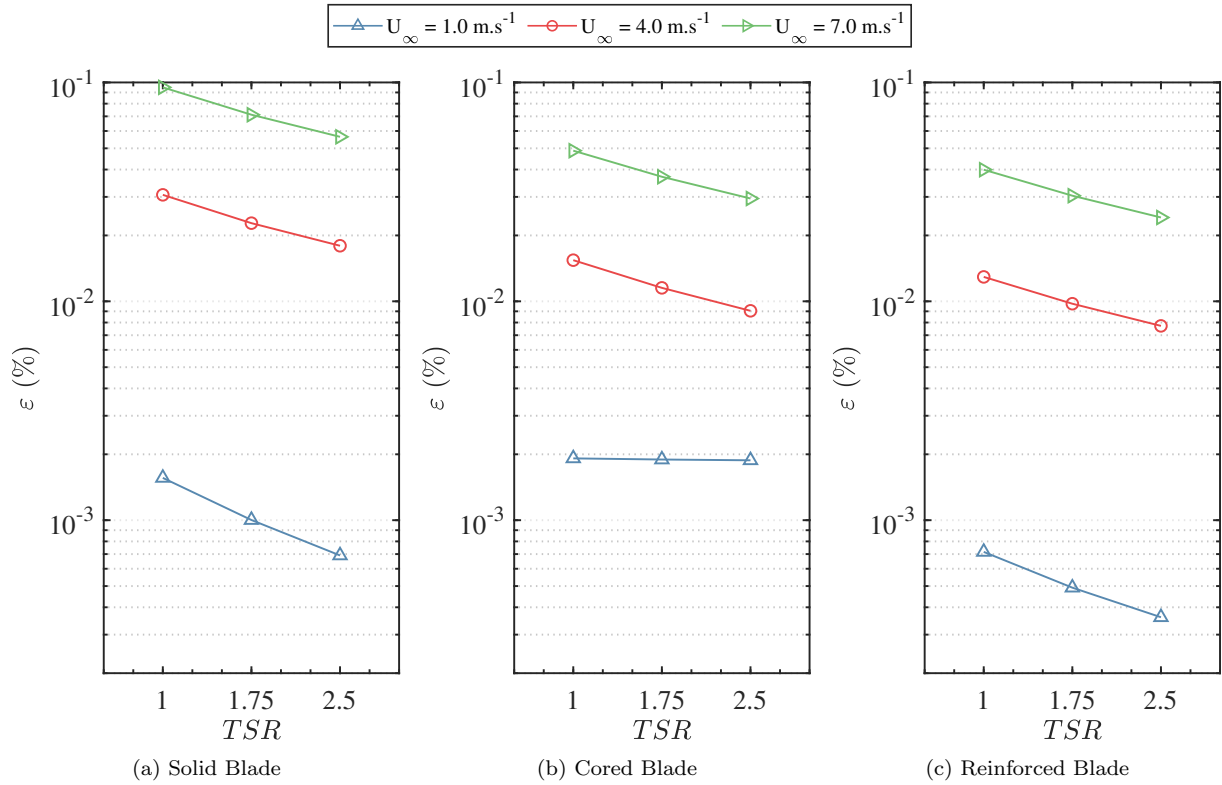


Figure 16: Mean normal axial strain of the distinct blade designs within aligned flow conditions

erties of the material utilised, namely the fatigue strength exponent (b) and fatigue strength parameter (σ'_f), to acquire the strain fluctuation that induces failure by fatigue within a number of cycles. The two values are typically established by means of experimentation in relation to destructive testing, which were not known for the adopted composite material. In this regard, as the supplementary terms within the strain-life equation were acquired, the methodology was therefore utilised to establish a definitive material property range to avoid failure by fatigue. The equation was satisfied by implementing the mean variation in principal elastic strain per cycle ($\Delta\varepsilon_e$) acquired via the finite-element analysis, Young's modulus (E), and number of cycles to failure (N_f) established to vary **between 10 to 25 years of operation within Paimpol-Bréhat site conditions [29]**.

The fatigue strength exponent for the reinforced design was computed in relation to the fatigue strength parameter when succumb to aligned and nominal yawed flow conditions at mid and high rotational velocities. By means of the range comparison, illustrated in Figure 21, the maximum fatigue strength exponent was acknowledged to occur at mid rotational velocities within nominal free-stream bearings.

Additionally, the material properties for the solid blade design was investigated, presented in Figure 22. In comparison to the reinforced design, the temporal response lessened as the solid design portrayed higher rigidity. Similar to the reinforced design, the maximum fatigue strength exponent occurred at mid rotational velocities within nominal free-stream

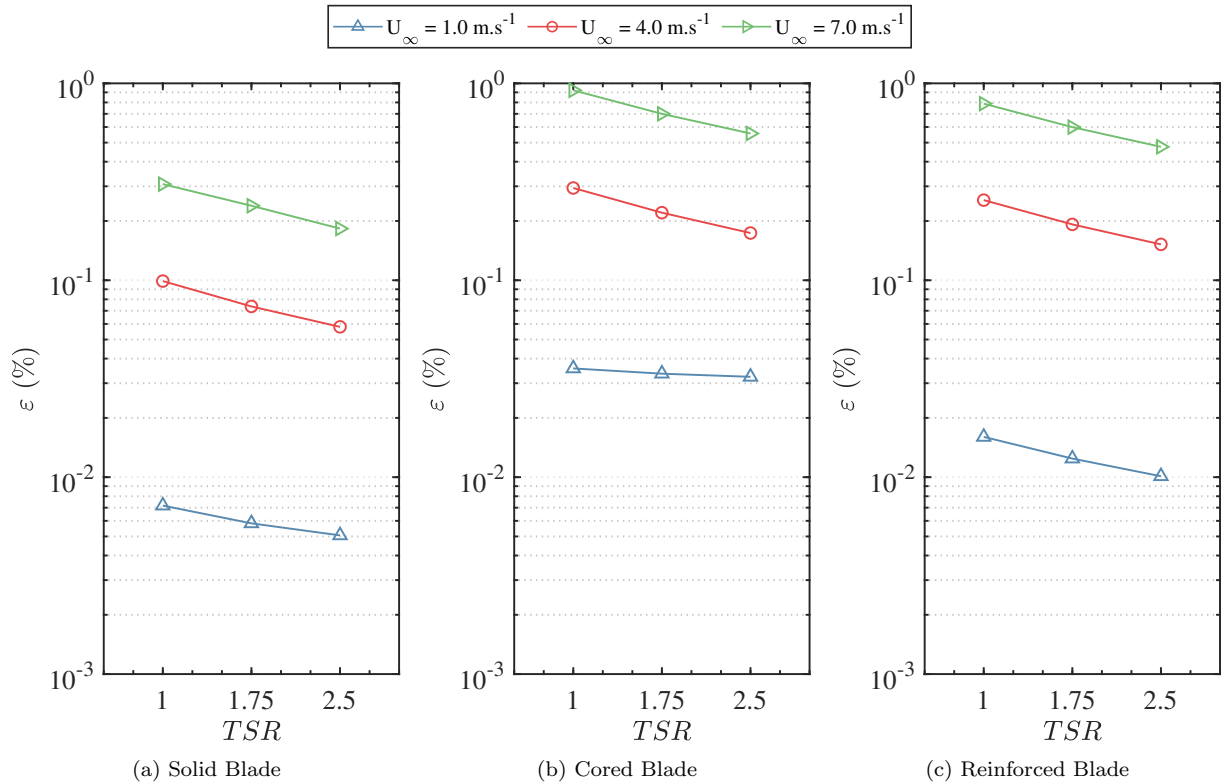


Figure 17: Mean equivalent strain of the distinct blade designs within aligned flow conditions

bearings. The material properties acknowledged for both designs were quasi-equivalent at mid and high rotational velocities. Despite establishing diminished forces upon the blades at the latter condition, the load cycle frequency was greater, hence contributing to the fatigue response.

In recognition of the temporal analyses, the variation in fatigue strength exponent, by considering the solid and reinforced internal blade designs through a 10 to 25-year design life within aligned and nominal flow bearings at mid and high rotational velocities, ranged from -0.24 to -0.46. In consideration that a fatigue strength exponent of -0.119 had been attained at a fatigue strength parameter of 557 MPa for a GFRP [30], the modelled outcomes were acknowledged to fall within a rational arrangement.

5. Conclusion

This study put forward an investigation into the structural response of a ducted, high-solidity tidal turbine rotor in real flow conditions by means of a partitioned-approach numerical coupling between a blade-resolved, unsteady computational fluid dynamics solver and a finite-element solver. The research strived to overcome the limitations of prior analyses by acknowledging the explicit three-dimensional physicality of the rotor blades. By this means, static pressure and wall shear-stress parameters were imported from the hydrodynamic model and mapped along the blade surface of the structural model as loading

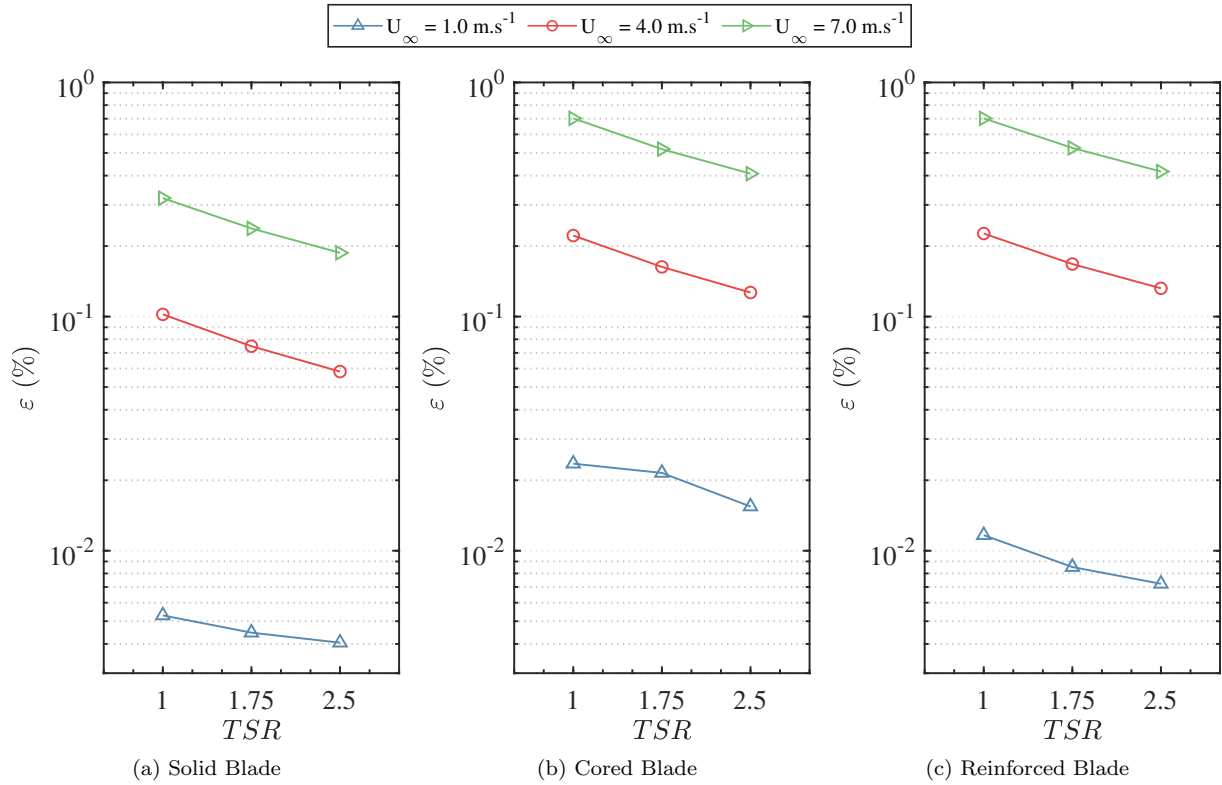


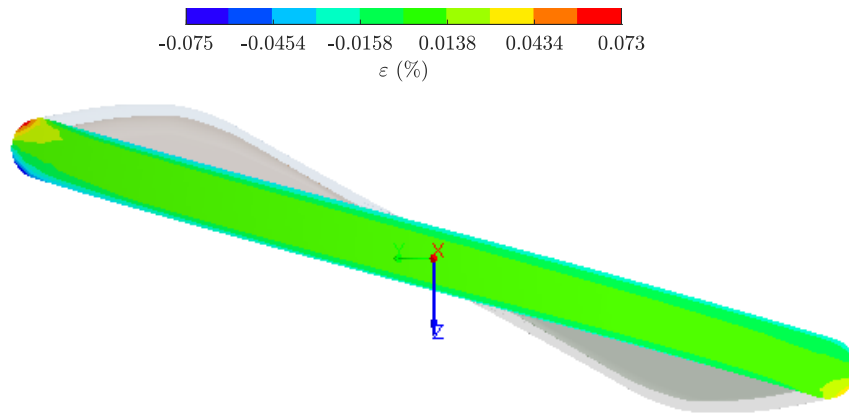
Figure 18: Mean shear strain of the distinct blade designs within aligned flow conditions

boundary conditions. As a result, a coherent representation of the turbine rotor blade response in aligned and yawed free-stream flows was established.

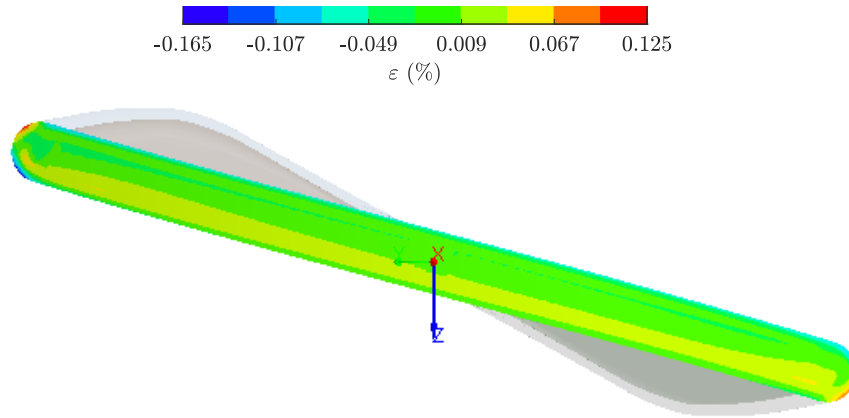
Three internal blade designs were put forward and analysed to acquire the more appropriate configuration for ducted, high-solidity rotor blades. In consideration of the structural outcomes derived, the geometrical characterisation of the three rotor designs was primarily acknowledged. The moment of inertia of the cored and reinforced blade were found to constitute 53.1% and 79.6% that of the solid blade, respectively. Subsequently, a hydrostatic analysis was undertaken to determine the structural integrity of the three blade designs at the installation water depth. All designs were acknowledged to sustain integrity, despite slight yielding apparent upon the cored design.

In continuation, a hydrodynamic analysis was undertaken. The highest normal strain response was induced by the cored blade design, portraying least rigidity, whereas the solid blade design attained the least response. The reinforced blade design provided an intermediate value. The investigated conditions were found to not exceed the ultimate strain value of the double-biased glass-fibre reinforced polymer for all blade designs. Due to the outcomes, the three designs were deemed to be largely equivalent in sustaining structural integrity at the operational conditions. Despite the outcomes, strain concentrations were induced at the leading edge of the blade, within the immediate vicinity of the root. This occurred upon all three structural blade designs in all flow conditions. The concentrations resulted from the

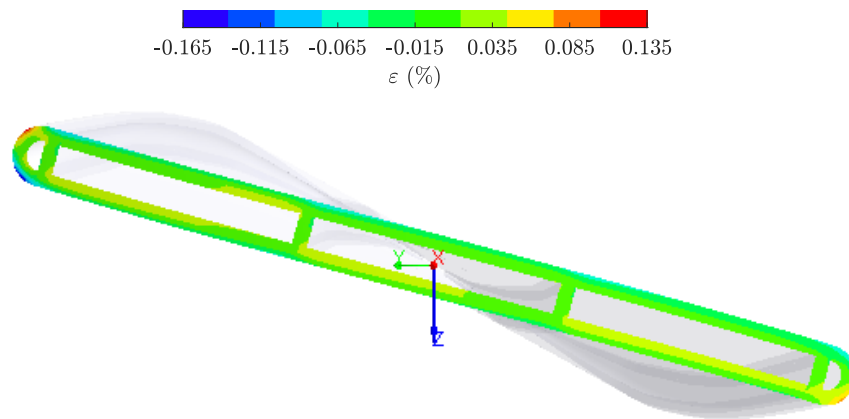
1
2
3
4
5
6
7
8
9
10
11
12
13
14
15
16
17
18
19
20
21
22
23
24
25
26
27
28
29
30
31
32
33
34
35
36
37
38
39
40
41
42
43
44
45
46
47
48
49
50
51
52
53
54
55
56
57
58
59
60
61
62
63
64
65



(a) Solid Blade



(b) Cored Blade



(c) Reinforced Blade

Figure 19: Illustrations of the shear strain distribution at the blade root ($U_\infty = 4 \text{ m.s}^{-1}$; $TSR = 1.75$; $\phi = 0^\circ$)

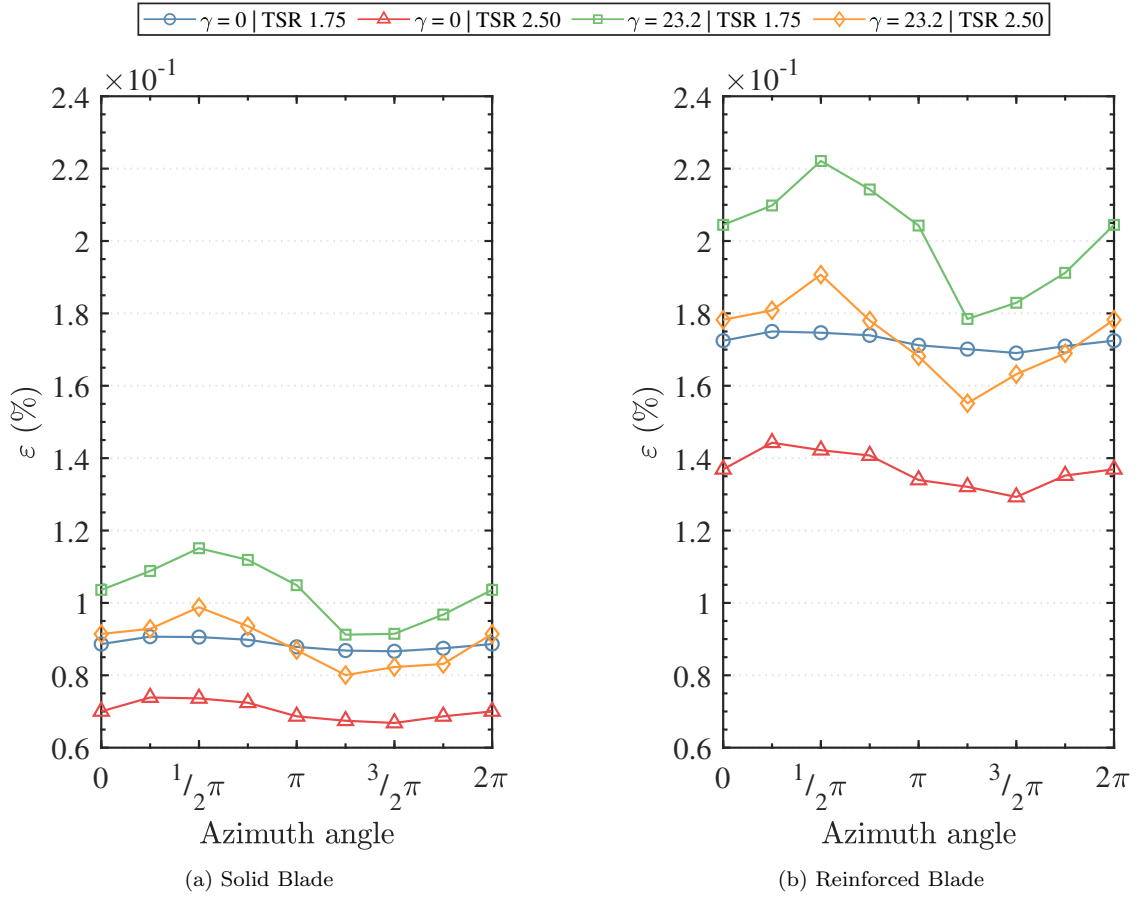


Figure 20: Cyclic representation of maximum equivalent strain of the distinct blade designs within aligned and yawed flow conditions

simultaneous bending and torsion responses.

Ancillary to the fracture analysis, a blade material cost analysis was undertaken to establish an estimation on the most cost-effective assortment of materials implementable for the three blade designs. The reinforced blade was acknowledged to require the least capital expenditure, whereas the solid blade required the highest.

In culmination, a fatigue analysis was undertaken to acknowledge an appropriate range of GFRP material properties for the designs within the considered flow conditions. By comparing the reinforced and solid blade designs, the values attained were found to be largely equivalent. Therefore, as a result of the outcomes attained and discussed, the reinforced internal blade design was considered to procure a favourable combination of high rigidity and comparatively lower weight, in addition to lower material capital expenditure. Albeit the outcome, further investigations are required to pursue a more appropriate design, specifically in establishing the optimised shell and webbing thickness for the operational conditions analysed, to further improve the performance of the ducted, high-solidity tidal turbine.

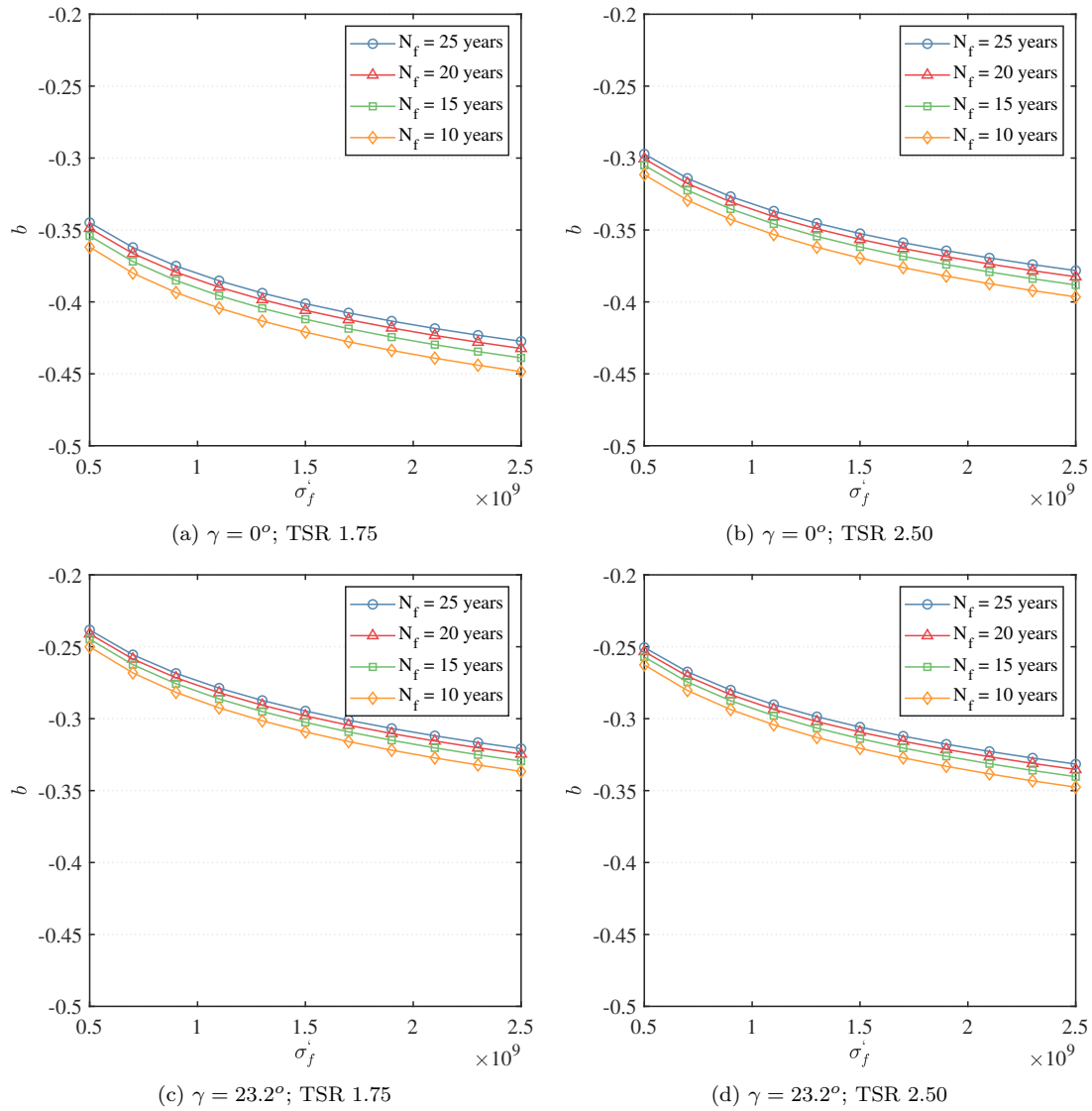


Figure 21: Fatigue response of the reinforced high-solidity tidal turbine rotor blade design

Acknowledgements

The research work disclosed in this publication is partially funded by the Endeavour Scholarship Scheme (Malta). Scholarships are part-financed by the European Union – European Social Fund (ESF) – Operational Programme II – Cohesion Policy 2014-2020: *“Investing in human capital to create more opportunities and promote the well-being of society”*.

Results were obtained using ARCHIE-WeSt High Performance Computer (www.archie-west.ac.uk).

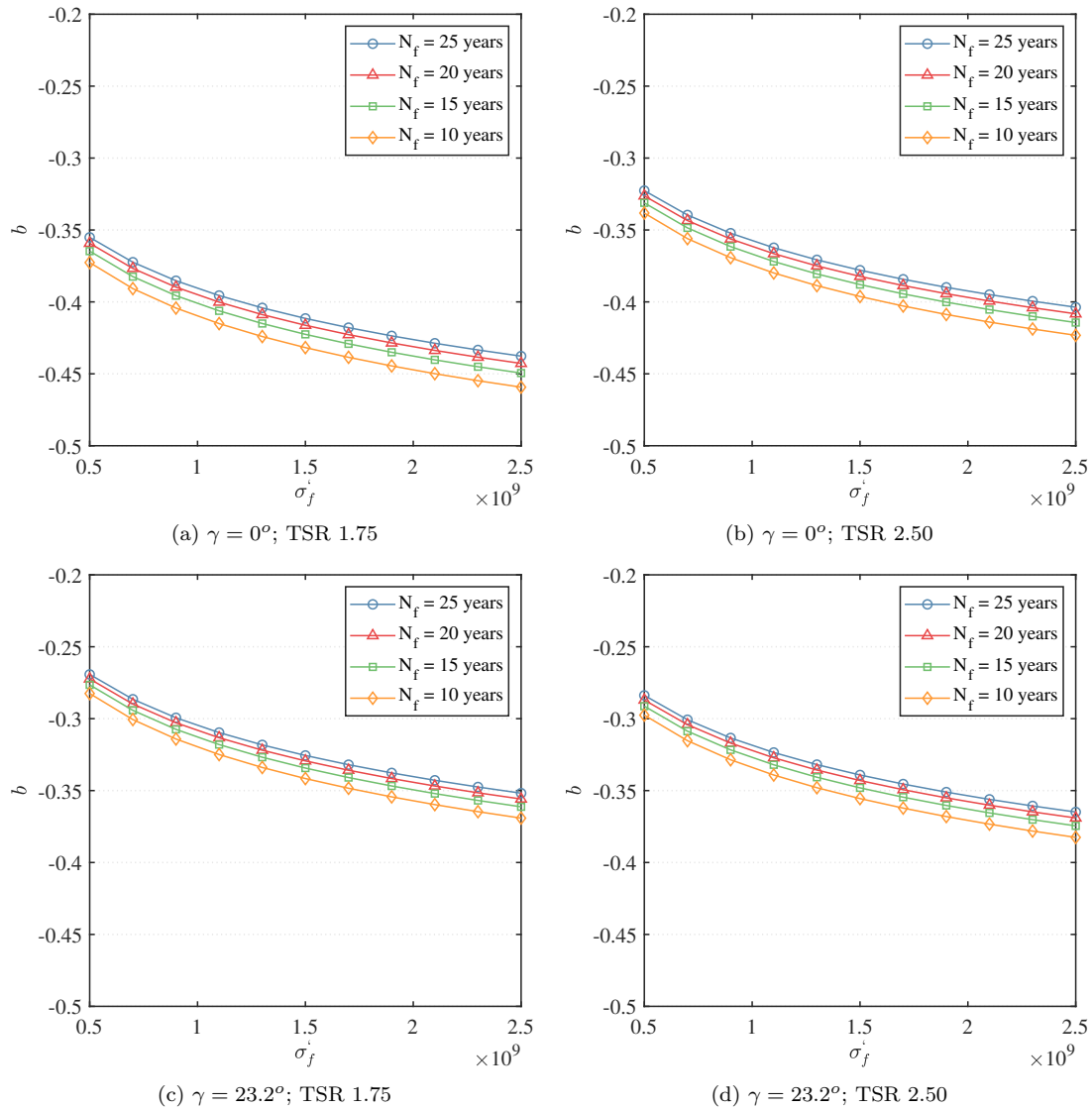


Figure 22: Fatigue response of the solid high-solidity tidal turbine rotor blade design

References

- [1] F. O'Rourke, F. Boyle, and A. Reynolds, "Tidal energy update 2009," *Applied Energy*, vol. 87, no. 2, pp. 398–409, 2010.
- [2] A. Kogan and A. Seginer, "T.A.E. Rep. No. 32A: Final report on shroud design," tech. rep., Department of Aeronautical Engineering, Technion – Israel Institute of Technology, Haifa, Israel, 1963.
- [3] M. G. Borg, Q. Xiao, S. Allsop, A. Incecik, and C. Peyrard, "A numerical performance analysis of a ducted, high-solidity tidal turbine," *Renewable Energy*, vol. 159, pp. 663 – 682, 2020.
- [4] M. G. Borg, Q. Xiao, S. Allsop, A. Incecik, and C. Peyrard, "A numerical swallowing-capacity analysis of a vacant, cylindrical, bi-directional tidal turbine duct in aligned & yawed flow conditions," *Journal of Marine Science and Engineering*, vol. 9, no. 2, 2021.
- [5] Bloomberg L.P., "OpenHydro Group Limited: Private Company Information - Bloomberg."

- 1
2
3
4 502 <https://www.bloomberg.com/profile/company/4074464Z:ID2018>. [Online; accessed 24 December
5 503 2020].
- 6 504 [6] OpenHydro Group Ltd., “Projects.” <http://www.openhydro.com/Projects>. [Online; accessed 13 August
7 505 2017].
- 8 506 [7] M. Nachtane, M. Tarfaoui, D. Saifaoui, A. E. Moumen, O. Hassoon, and H. Benyahia, “Evaluation of
9 507 durability of composite materials applied to renewable marine energy: Case of ducted tidal turbine,”
10 508 *Energy Reports*, vol. 4, pp. 31 – 40, 2018.
- 11 509 [8] S. Allsop, C. Peyrard, P. Bousseau, and P. Thies, “Adapting conventional tools to analyse ducted and
12 510 open centre tidal stream turbines,” *International Marine Energy Journal*, vol. 1, no. 2, pp. 91–99, 2018.
- 13 511 [9] R. Luquet, D. Bellevre, D. Fréchou, P. Perdon, and P. Guinard, “Design and model testing of an
14 512 optimized ducted marine current turbine,” *International Journal of Marine Energy*, vol. 2, pp. 61–80,
15 513 6 2013.
- 16 514 [10] H. Boudounit, M. Tarfaoui, D. Saifaoui, and M. Nachtane, “Structural analysis of offshore wind turbine
17 515 blades using finite element method,” *Wind Engineering*, vol. 44, no. 2, pp. 168–180, 2020.
- 18 516 [11] A. Betz, “Windmills in the light of modern research,” tech. rep., National Advisory Committee for
19 517 Aeronautics, Washington, DC, 8 1928.
- 20 518 [12] S. Allsop, C. Peyrard, P. R. Thies, E. Boulougouris, and G. P. Harrison, “Hydrodynamic analysis of a
21 519 ducted, open centre tidal stream turbine using blade element momentum theory,” *Ocean Engineering*,
22 520 vol. 141, pp. 531–542, 9 2017.
- 23 521 [13] The Canadian Press, “Cape Sharp Tidal turbine in Bay of Fundy now being monitored re-
24 522 motely.” [https://www.cbc.ca/news/canada/nova-scotia/cape-sharp-tidal-turbine-remote-monitoring-](https://www.cbc.ca/news/canada/nova-scotia/cape-sharp-tidal-turbine-remote-monitoring-environment-1.4814069)
25 523 [environment-1.4814069](https://www.cbc.ca/news/canada/nova-scotia/cape-sharp-tidal-turbine-remote-monitoring-environment-1.4814069), 2018. [Online; accessed 15 September 2018].
- 26 524 [14] G. M. Lilley and W. J. Rainbird, “A preliminary report on the design and performance of ducted
27 525 windmills,” Tech. Rep. 102, College of Aeronautics, Cranfield, Bedfordshire, United Kingdom, 04 1956.
- 28 526 [15] C. Belloni, R. Willden, and G. Houlby, “An investigation of ducted and open-centre tidal turbines
29 527 employing CFD-embedded BEM,” *Renewable Energy*, vol. 108, pp. 622–634, 2017.
- 30 528 [16] S. C. Allsop, *Hydrodynamic Modelling for Structural Analysis of Tidal Stream Turbine Blades*. PhD
31 529 thesis, University of Edinburgh, 6 2018.
- 32 530 [17] D. Grogan, S. Leen, C. Kennedy, and C. Bradaigh, “Design of composite tidal turbine blades,” *Renew-*
33 531 *able Energy*, vol. 57, pp. 151–162, 9 2013.
- 34 532 [18] M. Leong, L. C. Overgaard, O. T. Thomsen, E. Lund, and I. M. Daniel, “Investigation of failure
35 533 mechanisms in gfrp sandwich structures with face sheet wrinkle defects used for wind turbine blades,”
36 534 *Composite Structures*, vol. 94, no. 2, pp. 768 – 778, 2012.
- 37 535 [19] R. Barnes and E. Morozov, “Structural optimisation of composite wind turbine blade structures with
38 536 variations of internal geometry configuration,” *Composite Structures*, vol. 152, pp. 158 – 167, 2016.
- 39 537 [20] J. Zhu, X. Ni, and X. Shen, “Aerodynamic and structural optimization of wind turbine blade with
40 538 static aeroelastic effects,” *International Journal of Low-Carbon Technologies*, vol. 15, no. 1, pp. 55–64,
41 539 2019.
- 42 540 [21] J. Zhang, L. Guo, H. Wu, A. Zhou, D. Hu, and J. Ren, “The influence of wind shear on vibration
43 541 of geometrically nonlinear wind turbine blade under fluid–structure interaction,” *Ocean Engineering*,
44 542 vol. 84, pp. 14 – 19, 2014.
- 45 543 [22] R. Rafiee, M. Tahani, and M. Moradi, “Simulation of aeroelastic behavior in a composite wind turbine
46 544 blade,” *Journal of Wind Engineering and Industrial Aerodynamics*, vol. 151, pp. 60 – 69, 2016.
- 47 545 [23] L. Krstulovic-Opara, B. Klarin, and Z. Domazet, “A non-destructive wind turbine blade analysis based
48 546 on the Thermal Stress Analysis,” (Split, Hrvatska), 2009.
- 49 547 [24] D. C. Wilcox, *Turbulence Modeling for CFD, Third Edition*. San Diego: DCW Industries, Inc, third ed.,
50 548 2006.
- 51 549 [25] Z. Zhou, M. Benbouzid, J.-F. Charpentier, F. Sculler, and T. Tang, “Developments in large marine
52 550 current turbine technologies – a review,” *Renewable and Sustainable Energy Reviews*, vol. 71, pp. 852
53 551 – 858, 2017.
- 54 552 [26] Resistance Committee of the 28th ITTC., “Uncertainty Analysis in CFD Verification and Validation,
55
56
57
58
59
60
61
62
63
64
65

1
2
3
4
5
6
7
8
9
10
11
12
13
14
15
16
17
18
19
20
21
22
23
24
25
26
27
28
29
30
31
32
33
34
35
36
37
38
39
40
41
42
43
44
45
46
47
48
49
50
51
52
53
54
55
56
57
58
59
60
61
62
63
64
65

553 Methodology and Procedures.” Technical Report. ITTC: Zürich, Switzerland, 2017.

554 [27] P. Bortolotti, D. Berry, R. Murray, E. Gaertner, D. Jenne, R. Damiani, G. Barter, and K. Dykes, “A
555 Detailed Wind Turbine Blade Cost Model,” Tech. Rep. NREL/TP-5000-73585, National Renewable
556 Energy Laboratory, Golden, Colorado, June 2019.

557 [28] Solvay S.A., “MTM 28 SERIES.” <https://www.solvay.com/en/product/mtm-28>, 2013. [Online; ac-
558 cessed 22 November 2019].

559 [29] C.-T. Pham and V. A. Martin, “Tidal current turbine demonstration farm in Paimpol-Brehat (Brit-
560 tany): tidal characterisation and energy yield evaluation with Telemac,” in *Proceedings of the 8th*
561 *European Wave and Tidal Energy Conference, Uppsala, Sweden*, vol. 710, 2009.

562 [30] C. Manjunatha, A. Taylor, A. Kinloch, and S. Sprenger, “The tensile fatigue behaviour of a silica
563 nanoparticle-modified glass fibre reinforced epoxy composite,” *Composites Science and Technology*,
564 vol. 70, no. 1, pp. 193–199, 2010.



[Click here to access/download](#)

LaTeX Source Files

Structural analysis of blade (1).zip

